Scripta Materialia 269 (2025) 116912

Contents lists available at ScienceDirect

Scripta Materialia

journal homepage: www.journals.elsevier.com/scripta-materialia

Prolonged martensitic transformation induced by heterogeneous deformation in a heterostructured metastable high-entropy alloy

Kejie Lu [a], Xinkai Ma [a,*], Yuntian Zhu [b]

[a] Key Laboratory of Advanced Technologies of Materials, Ministry of Education, School of Materials Science and Engineering, Southwest Jiaotong University, Chengdu, Sichuan 610031, China
[b] Department of Materials Science & Engineering, City University of Hong Kong, Kowloon, 999077, Hong Kong, China

ARTICLE INFO

Keywords:
Heterostructure
Metastable high-entropy alloy
Heterogeneous deformation
Shear bands
Martensitic transformation

ABSTRACT

We report prolonged martensitic transformation in heterostructured metastable high-entropy alloy composed of non-recrystallized (NRX) and recrystallized ultrafine-grained (UFG) zones. This distinctive transformation behavior is attributed to heterogeneous deformation inherent in heterostructures. The high stress concentrations at the hetero-zone boundaries facilitate preferential nucleation and stable evolution of martensite within the NRX zones. This process accommodates stress localization and establishes a pronounced strain gradient between the NRX and UFG zones. Additionally, the activation of shear bands, driven by the high dislocation density in the UFG zones, initiates and extends the martensitic transformation to higher strain levels. As a result, this prolonged martensitic transformation significantly extends high work-hardening into high applied strains, thereby producing an excellent strength-ductility combination.

To overcome the dilemma of the strength-ductility trade-off, the concept of heterostructure has recently attracted significant attention [1]. Heterostructures typically consist of hard and soft zones that exhibit significant mechanical incompatibility [2,3]. Metallic materials with heterostructures promote geometrically necessary dislocations (GNDs) accumulation at hetero-boundary affected regions (HBars) during plastic deformation. This process introduces hetero-deformation-induced (HDI) strengthening and hardening, demonstrating potential for superior strength-ductility combinations [4–6]. However, these beneficial strengthening effects are closely related to the internal microstructure, particularly the structural characteristics of the hard zones [7,8]. Therefore, heterostructured materials with high-strength and ductility often require meticulous microstructural design.

Stress-induced martensitic transformation in metastable alloys may provide a wide process window for heterostructural design [1,9–12]. This is attributed to the transformation-induced plasticity (TRIP) effect, which can optimize the work hardening behavior of heterostructured materials [13]. Therefore, it is logical to combine these two important strategies (heterostructure and metastable engineering) to fabricate heterostructure, which can potentially obtain better performance. Indeed, Kim et al. [14] demonstrated the possibility of achieving multi-stage work-hardening behavior and superior strength-ductility balance by using partial recrystallization annealing to prepare heterostructure in metastable medium-entropy alloy. Ran et al. [15]. prepared heterostructure with different metastable zones in stainless steel, exhibiting high work-hardening capability while maintaining large uniform elongation and providing exceptionally high yield strength. Similarly, Lu et al. [16]. mitigated the embrittlement caused by the σ phase in high-entropy alloy (HEA) by using the combination of TRIP effects and heterostructure, developing high-strength and tough HEA. However, the phase transformation behavior and its synergistic mechanism between the constituent zones in heterostructure has not been well studied, especially in metastable HEA.

To investigate these issues, we studied the plastic deformation behavior of the non-recrystallized (NRX) zones and recrystallized ultrafine-grained (UFG) zones in heterostructured metastable HEA, aiming to reveal martensitic transformation mechanisms in constituent zones. This work reveals the prolonged martensitic transformation in the heterostructured metastable HEA, driven by heterogeneous deformation. Such deformation alleviates the inhibition of martensite transformation by the NRX zones (high-density dislocation) and the UFG zones, and leads to a continuous martensite transformation from the NRX to UFG zones. This prolonged martensitic transformation enables the TRIP effect to be exploited over a wider strain range rather than

* Corresponding author.
E-mail address: sdutmakai@swjtu.edu.cn (X. Ma).

https://doi.org/10.1016/j.scriptamat.2025.116912
Received 20 April 2025; Received in revised form 8 July 2025; Accepted 3 August 2025
Available online 6 August 2025

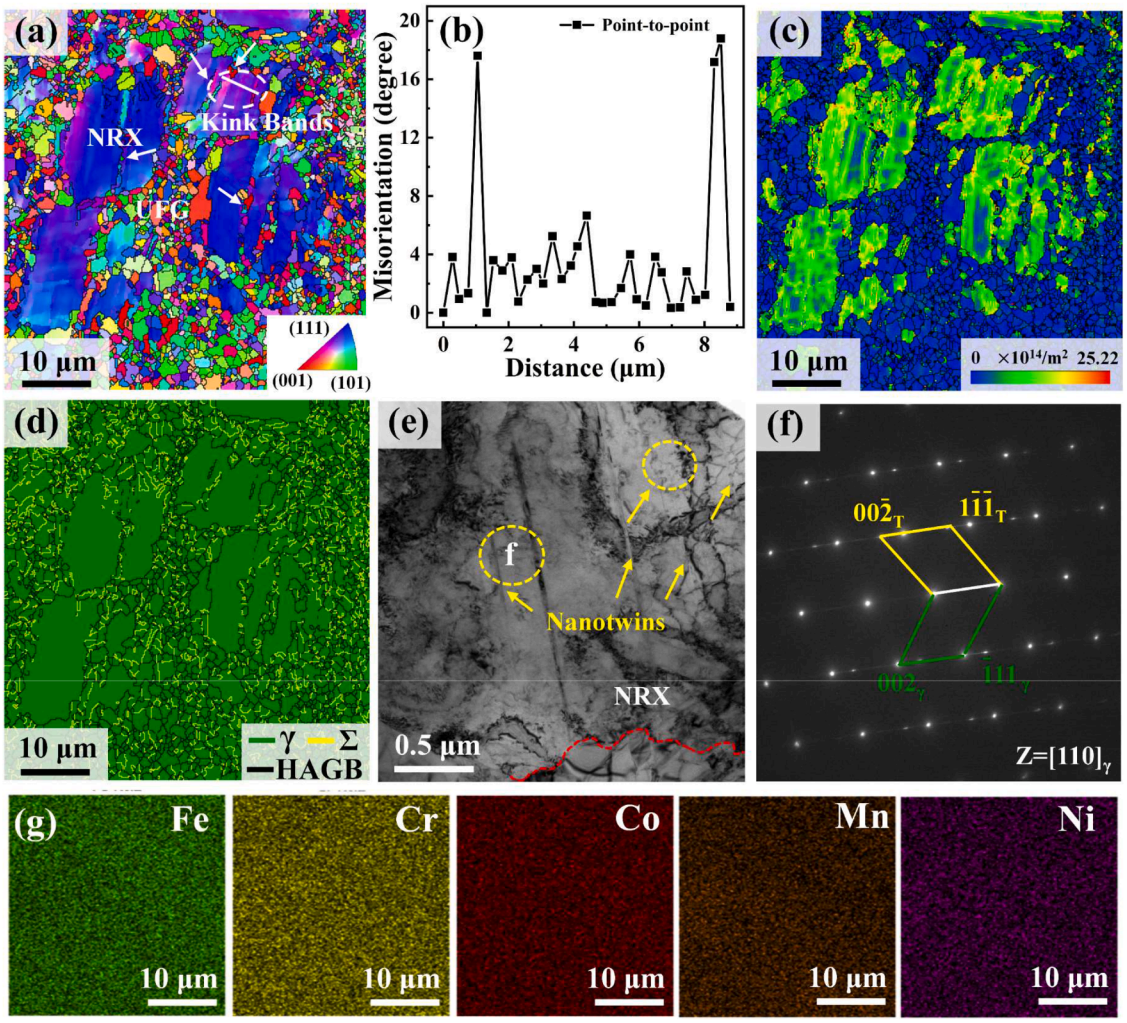

Fig. 1. Initial microstructure of the heterostructured metastable HEA: (a) Inverse pole figure (IPF) map and (b) is misorientation profile along the solid line across the kink bands in (a). (c) GND density map. (d) Phase map. (e) and (f) Representative TEM images. (g) Energy dispersive spectrometer maps. Where γ, Σ and HAGB refer to FCC phase, twin boundary and high-angle grain boundary (>15°), respectively.

occurring at low strain levels.

The as-cast $Fe_{40}Co_{20}Cr_{20}Mn_{10}Ni_{10}$ metastable HEA used in this work was prepared by vacuum induction levitation melting furnace. To ensure chemical homogeneity, the ingot was remelted at least five times. The as-cast metastable HEA exhibited an average grain size of 35.4 ± 0.20 μm with predominantly FCC phase (Supplementary Figs. S1 , S2). Final chemical compositions were determined using energy dispersive spectrometer and listed in Supplementary Table S1. The as-cast metastable HEA was subjected to multiple cold rolling passes with a thickness reduction of 0.1 mm per pass, decreasing from 5 mm to 0.5 mm (45 passes, 90 % reduction). After rolling deformation, the martensite content of the metastable HEA increased to ~68.1 %. To fabricate heterostructured metastable HEA, the as-rolled metastable HEA was annealed at 600 °C for 10 min followed by water quenching. From the XRD patterns and the evolution of martensite content (Supplementary Fig. S2), the reverse transformation from martensite to FCC phase in heterostructure was completed after annealing.

Dog-bone-shaped tensile samples were cut along the rolling direction, with a gauge length of 7.5 mm, a width of 3 mm, and a thickness of 0.5 mm. The uniaxial tensile tests were conducted on a universal testing machine at a strain rate of 10^{-3} s^{-1}. XRD measurements were performed on the Pro MPD XRD diffractometer to obtain the martensite content under different processing conditions. The microstructural evolution at different strain levels were characterized using electron backscatter diffraction (EBSD, FEI Quanta FEG 250) and transmission electron microscopy (TEM, both FEI Titan Cube 80–300 and JEOL JEM-2100F). Geometrically necessary dislocation (GND) density calculations were carried out in the EBSD analysis software. The detailed calculation method is in Supplementary Material.

Fig. 1 shows the EBSD and TEM analysis of the heterostructured metastable HEA. The heterostructured metastable HEA contains NRX and UFG zones, exhibiting an FCC single-phase structure (Fig. 1d) and uniform elemental distribution (Fig. 1*g*). The NRX zones are primarily composed of large grains, while the UFG zones show equiaxed grain with an average grain size of ~0.72 ± 0.10 μm. Kink bands with a crystallographic misorientation of 5°−20° are present in the NRX zones (Fig. 1a), consistent with previous reports [17,18]. The presence of UFGs within and around the kink bands (Fig. 1a, marked with white arrows) suggests that its nucleation mechanism may be similar to that of shear bands (SBs). This is because the kink bands also exhibit higher GND density ($10.3 \times 10^{14}/m^2$) than surrounding matrix ($7.0 \times 10^{14}/m^2$), evidenced by the GND density map in Fig. 1c.

The highly concentrated plastic deformation enables the kink bands to serve as nucleation sites for static recrystallization, which contributes to formation of heterostructure during annealing [19,20]. Additionally, high-density nanotwins are observed within the NRX zones (Fig. 1f), which are confirmed by twin diffraction spots in the SAED pattern. These nanotwins are mainly formed by the reverse transformation from

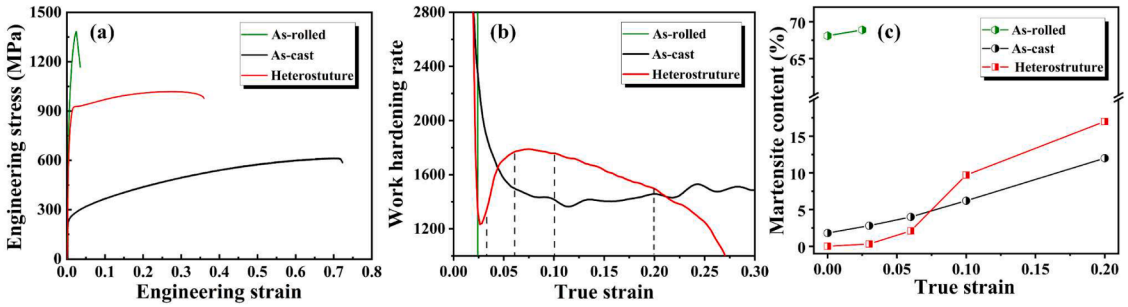

Fig. 2. Mechanical performance and martensitic transformation of the metastable HEA: (a) Engineering stress-strain curves. (b) work hardening rate curves. (c) Comparison of martensite content under different tensile strains.

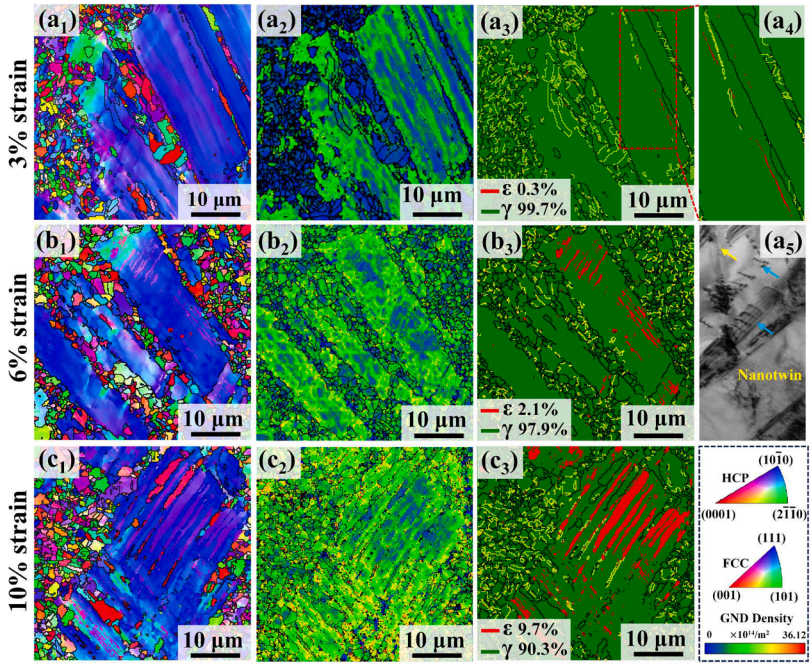

Fig. 3. Microstructure evolution of the heterostructured metastable HEA at ~3 %, ~6 % and ~10 % tensile strain: (a_1-c_1) IPF maps. (a_2-c_2) GND density maps. (a_3-c_3) Phase maps. (a_5) Representative TEM image of the NRX zones. Where ε refers to martensite.

martensite to FCC twins through the recombination of partial dislocations, facilitated by the low stacking fault energy of the alloy [21]. In contrast, the UFG zones exhibit the typical characteristics of recrystallized grain, namely small grain size and low defect density.

Fig. 2 compares the tensile properties of the metastable HEA under different processing conditions. The as-cast metastable HEA exhibits a high uniform elongation of ~70.0 %, but its yield strength is only ~255.0 MPa. After rolling, the yield strength of the as-rolled metastable HEA increases to ~1382.6 MPa, but the uniform elongation drops sharply to ~2.3 %. This demonstrates a typical strength-ductility trade-off. In contrast, the heterostructured metastable HEA exhibits a high yield strength of ~922.5 MPa, which is 3.6 times that of the as-cast metastable HEA, while maintaining a large uniform elongation of ~27.1 %. Therefore, the heterostructured metastable HEA exhibits excellent strength-ductility combination.

It is noteworthy that the hardening rate of the heterostructured metastable HEA shows an upturn (~2.6 %) after an initial decrease, and then remains at a level higher than that of the as-cast metastable HEA until ~21 % true strain (Fig. 2b). The high work hardening capacity of the heterostructure is related to the enhanced martensitic transformation ability, as shown in Fig. 2c. However, this enhanced phase transformation capability potentially stems from the prolonged martensitic transformation in the heterostructured metastable HEA, which is driven by heterogeneous deformation between constituent zones.

Table 1
GND density in the NRX and UFG zones at different tensile strain.

Zone	GND density (10^{14}/m^2)				
	0 %	3 %	6 %	10 %	Increment after 10 %
NRX	8.7	9.3	8.5	12	3.3
UFG	0.7	4.5	6.4	8.9	8.2

To elucidate the phase transformation behavior induced by heterogeneous deformation in different zones, we conducted EBSD analysis for the heterostructured metastable HEA at ~3 %, ~6 %, and ~10 % tensile strain (Fig. 3). There is a significant difference in GND density between the hetero-zone boundaries at different strain levels (Fig. 3a_2-c_2), indicating that large strain gradient is formed during deformation. Additionally, compared to the initial microstructure, the increment in GND density for NRX zones and UFG zones are 3.3×10^{14}/m^2 and 8.2×10^{14}/m^2 at 10 % tensile strain (Table 1), respectively, indicating that severe plastic heterogeneity is developed in the heterostructured metastable HEA. The UFG zones have undergone more plastic deformation and act as soft zones, while NRX zones serve as hard zones.

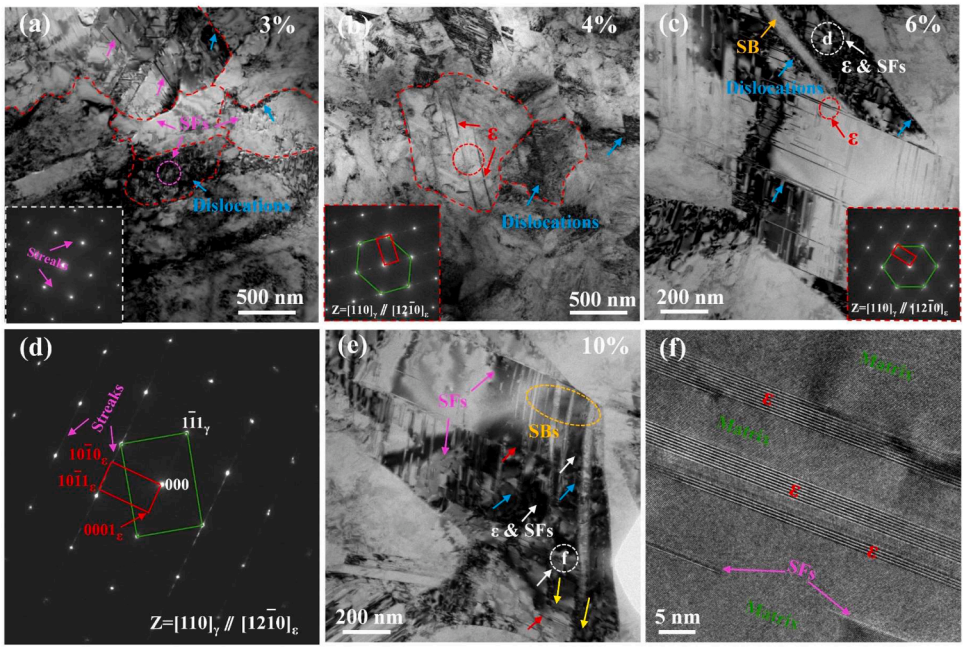

Fig. 4. TEM images of UFG zones at ~3 %, ~4 %, ~6 % and ~10 % tensile strain: (a) Only the activity of SFs and dislocations in the UFG zones. (b) A small amount of martensite. (c) Awakening martensitic transformation by nucleation of shear bands (SBs). (d) SAED pattern proves the existence of martensite at the edge of SBs. (e) High-density SBs induced abundant martensitic transformation. (f) High-resolution pattern from (e).

The serve heterogeneous deformation of heterostructured metastable HEA mainly stems from the mechanical incompatibility between the aforementioned NRX and UFG zones, which will affect the stress distribution at the hetero-zone boundaries. Due to the deformation constraint caused by elastic NRX zones, the soft UFG zones cannot deform freely in an elastic-plastic transition stage [22]. Consequently, the GNDs are blocked and accumulation near the hetero-zone boundaries in the UFG zones (Fig. 3a_2), resulting in the formation of long-range internal stresses, i.e. back stresses in the UFG zones and forward stresses in the NRX zones [23,24]. Before yielding, the long-range internal stresses increase with the accumulation of GNDs, which lead to high stress concentrations at the hetero-zone boundaries [25,26].

The high stress concentrations at the hetero-zone boundaries produces forward stresses in the neighboring NRX zones to promote activation of slip systems [23,27]. In this case, the pre-existing high-density dislocation (Fig. 1f) enables rapid stress elevation in the NRX zones, particularly at their boundaries (Fig. 3a_2). This high-stress also provides the driving force for martensitic transformation [27,28]. In addition, the nanotwins in the NRX zones pose the nucleation sites for martensite. This is because when dislocations impinge on the nanotwins boundaries, the leading Shockley dislocations may dissociate into stair-rod and glissile partial dislocations (Fig. 3a_5), thus facilitating formation of martensite at the nanotwins boundaries [29,30]. Therefore, compared to the UFG zones, the NRX zones preferentially undergo martensitic transformation (Fig. 3a_3& a_4).

Interestingly, martensite variant is observed in the NRX zones at ~6 % tensile strain, with misorientation of ~70.5° from the early formation (Fig. 3b3). Notably, the newly formed martensite effectively releases the high local stress, as evidenced by the decrease in GND density in the phase transformation zone (Fig. 3b_2). The martensite nucleates and grows further along the nanotwin boundaries in the NRX zones during subsequent deformation (~10 %), resulting in martensite dispersion over almost the whole zones (Fig. 3c_3). In this case, the local stress released by martensite formation can still be observed, while simultaneously new GNDs are stored at martensitic boundaries (Fig. 3c_3). This indicates that the continuous formation of martensite in the NRX zones alleviates the localization of internal stress, thereby preventing premature failure due to localized instability during deformation.

The continuous martensitic transformation in the NRX zones facilitates the maintenance of the subsequent strain distribution, resulting in significant strain gradient from the NRX to the UFG zones (Figs. 3(a_2-c_2)). However, due to the limitations of EBSD resolution, we were unable to obtain more microscopic results to further understand the deformation behavior of the UFG zones under these micro strain gradients. Therefore, we conducted further analysis using TEM (Fig. 4). At the initial stage of deformation (~3 %), dislocation slip in the UFG zones is exceptionally active and tends to accumulate at the hetero-zone boundaries (Fig. 4a), which is consistent with the EBSD results. The back stress generated by the accumulation of dislocation allows the soft UFG zones to harden to the level of the NRX zones, thereby offsetting high applied stress. There is no stress-induced martensitic transformation in the UFG zones at ~3 % tensile strain, with only stacking faults (SFs). Therefore, compared to the NRX zones, the primary deformation behavior in the UFG zones during this stage remains extensive dislocation activity, while martensitic transformation is suppressed, which is attributed to high mechanical stability of the UFG zones [15]. In fact, martensitic transformation initiates in the UFG zones only upon reaching ~4 % tensile strain and is confirmed by SAED pattern (Fig. 4b).

However, compared with the NRX zones under the same strain level (Fig. S3), the martensitic transformation capability in the UFG zones remains low. Instead, the UFG zones tend to undergo plastic response of local instability, leading to the nucleation of SB (Fig. 4c), since the high-density dislocations introduced by the large strain gradient can only interact within a limited volume. Typically, traditional UFG materials often become plastically unstable due to an individual catastrophic SB, resulting in rapid necking [31,32]. Interestingly, the SBs observed here can restore the metastability of the UFG zones, as evidenced by the martensite and SFs around the SBs at ~6 % tensile strain (Fig. 4c). As the strain further increases to ~10 %, increased shear deformation is observed in the UFG zones, activating abundant martensite and SFs (Figs. 4e , f). Previous work has pointed out that SB boundaries can not only trap dislocations but also act as dislocations sources, further enhancing the local stress in the neighboring matrix [32,33]. This provides sufficient driving force to overcome the additional energy barrier imposed by the constraints of the UFG zones, thereby inducing martensitic transformation[34].

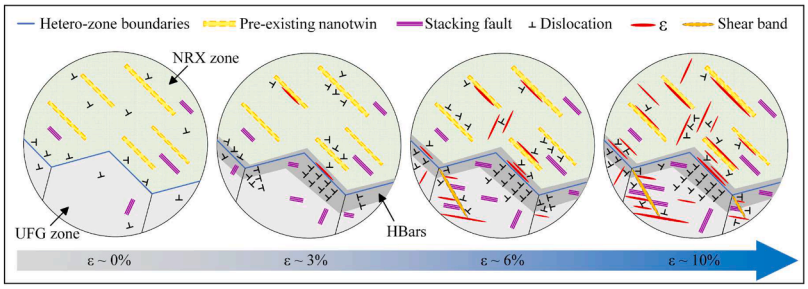

Fig. 5. Schematic diagram showing deformation mechanisms in the heterostructured metastable HEA under different tensile strain.

On the other hand, the martensite formed in the UFG zones spans the entire tip of the SBs (Figs. 4c , e), despite the presence of evidence indicating forward propagation of the SBs under large strains (Fig. 4e, marked with yellow arrow). We can infer that the martensite inhibits the SB propagation along the predetermined shear direction by relieving the stress concentration at the SB tip, thereby avoiding catastrophic fracture. In addition, the strain hardening induced by the martensitic transformation can also stabilize the SBs [35,36]. Consequently, the nucleation of SBs in the UFG zones during deformation does not lead to premature failure. Instead, the SBs can transform into stable SBs during continued loading, and provide the driving force for martensitic transformation in the UFG zones under high strain conditions.

Fig. 5 summarizes the microstructure evolution in the heterostructured metastable HEA by schematic diagram. With increasing strain, the martensite gradually forms from the NRX to UFG zones, which extends the phase transformation to large plastic strains, thereby inducing a prolonged martensitic transformation. This distinctive martensitic transformation mechanism is associated with heterogeneous deformation in the heterostructure. Theoretically, the high-density pre-existing dislocation in the alloy enhances the resistance to martensitic transformation by impeding the cooperative atomic movement [27,37]. However, in the current heterostructure, the pre-existing high-density dislocation in the NRX zones does not suppress the martensitic transformation. We find instead that preferential nucleation and stable expansion of martensite in the NRX zones, which can be attributed to the high stress concentration at hetero-zone boundaries resulting from the heterogeneous deformation. This high stress concentration produces a forward stress to increase the stress level within the NRX zones and enhances dislocation activity at the nanotwin boundaries, thereby creating favorable conditions for the continuous formation of martensite. The continuous martensitic transformation in the hard NRX zones prevents saturation strain hardening caused by the high-density defects, thereby accommodating the localization of stress and allowing for the sustained strain distribution within the heterostructure. Since the strain must be continuous, the soft UFG zones need to accumulate a substantial number of GNDs at their interiors to accommodate the development of strain gradients [11,38]. Considering the high mechanical stability of the UFG zones and the restricted dislocation activity space, the high-density dislocations exacerbate internal strain localization, leading to the nucleation of SBs. The formation of SBs and the stress accumulation at their boundaries overcome the inherent limitations of the UFG zones, and promote the nucleation of martensite under higher strains. This is different from the suppression of the TRIP effect in small-sized grains in heterostructures reported by Li et al. [39]. Therefore, our results reveal that this prolonged phase transformation from NRX to UFG zones enables the martensitic transformation to be distributed over a wide strain range, rather than concentrating at low strain levels. This avoids the rapid exhaustion of TRIP-assisted work hardening capacity and helps sustain high work hardening capability.

In summary. The heterogeneous deformation induces high stress concentrations at hetero-zone boundaries, elevating NRX zone stress and promoting dislocation activity at nanotwin boundaries. This enables preferential nucleation and stable expansion of martensite in NRX zones, thereby establishing a pronounced strain gradient. The high-density dislocations generated in the UFG zones lead to the formation of shear bands, which activate martensitic transformation under high strain. The prolonged martensitic transformation from NRX to UFG zones is responsible for the enhanced strain hardening capability. This work elucidates the influence mechanism of heterogeneous deformation on the phase transformation between constituent zones and provides valuable insights for achieving an excellent balance between strength-ductility.

CRediT authorship contribution statement

Kejie Lu: Writing – original draft, Data curation. **Xinkai Ma:** Writing – review & editing, Supervision, Funding acquisition, Formal analysis, Conceptualization. **Yuntian Zhu:** Writing – review & editing, Funding acquisition, Formal analysis.

Declaration of competing interest

The authors declare that they have no known competing financial interests or personal relationships that could have appeared to influence the work reported in this paper.

Acknowledgements

This work was supported by the National Key R&D Program of China (2021YFA1200202), the National Natural Science Foundation of China (Grant No. 52201142), the Sichuan Province Science and Technology Program (No. 2025YFHZ0230), and the Fundamental Research Funds for the Central Universities (Grant No. 2682024GF014). The authors are also grateful to the Analytical and Testing Center of Southwest Jiaotong University for TEM characterization.

Supplementary materials

Supplementary material associated with this article can be found, in the online version, at doi:10.1016/j.scriptamat.2025.116912.

References

[1] Y. Zhu, X. Wu, Prog. Mater. Sci. 131 (2023) 101019.
[2] X. Wu, M. Yang, F. Yuan, G. Wu, Y. Wei, X. Huang, Y. Zhu, Proc. Natl. Acad, Science 112 (47) (2015) 14501–14505.
[3] Z. Luo, T. Feng, X. Ma, Mater. Sci. Eng. A 936 (2025) 148420.
[4] Y. Zhu, X. Wu, Mater. Res. Lett. 7 (10) (2019) 393–398.
[5] J. Li, X. Ma, J. Zhou, C. Xu, P. Li, X. Tian, Q. Wang, H. Fan, Int. J. Plast. 192 (2025) 104410.
[6] X. Ma, P. Zhang, N. Li, Z. Luo, L. Yang, Mater. Sci. Eng. A 936 (2025) 148424.
[7] J. Fan, X. Ji, L. Fu, J. Wang, S. Ma, Y. Sun, M. Wen, A. Shan, Int. J. Plast. 157 (2022) 103398.
[8] Y. Jo, S. Jung, W. Choi, S. Sohn, H. Kim, B. Lee, N.J. Kim, S. Lee, Nat. Commun. 8 (1) (2017) 15719.
[9] R.E. Kim, G.H. Gu, S.Y. Ahn, Y.-U. Heo, J. Moon, Q. Wu, H. Chae, Y. Baik, W. Woo, H. Kwon, Acta Mater. 275 (2024) 120060.
[10] X. Wu, M. Yang, F. Yuan, L. Chen, Y. Zhu, Acta Mater. 112 (2016) 337–346.

[11] Q. Jia, L. Chen, X. Chen, H. Choi, Z. Xing, S. Lee, H. Kim, H. Wang, H. Huang, M. Jin, Scripta. Mater. 226 (2023) 115196.
[12] K. Lu, J. Li, Y. Wang, X. Ma, J. Alloy. Compd. 941 (2023) 168979.
[13] Q. Yang, D. Yan, Y. Zhang, K. Gan, Z. Li, Mater. Sci. Eng. A 894 (2024) 146224.
[14] J.W. Bae, J. Lee, A. Zargaran, H.S. Kim, Scripta. Mater. 194 (2021) 113653.
[15] R. Ding, Y. Yao, B. Sun, H. Guo, J. Zhang, Y. Shao, C. Zhang, W. Liu, A. Godfrey, Z. Yang, Scr. Mater. 252 (2024) 116274.
[16] W. Lu, W. Guo, Z. Wang, J. Li, F. An, G. Dehm, D. Raabe, C.H. Liebscher, Z. Li, Acta Mater. 246 (2023) 118717.
[17] S. Wang, S. Lu, M. Wu, D. Wang, G. Zhu, C. Yang, D. Shu, B. Sun, L. Vitos, Mater. Sci. Eng. A 832 (2022) 142476.
[18] J. Zhang, B. Qian, Y. Wu, Y. Wang, J. Cheng, Z. Chen, J. Li, F. Sun, F. Prima, J. Mater. Sci. Technol. 74 (2021) 21–26.
[19] J. Su, D. Raabe, Z. Li, Acta Mater. 163 (2019) 40–54.
[20] T. Sakai, A. Belyakov, R. Kaibyshev, H. Miura, J.J. Jonas, Prog. Mater. Sci. 60 (2014) 130–207.
[21] W. Lu, C.H. Liebscher, G. Dehm, D. Raabe, Z. Li, Adv. Mater. 30 (44) (2018) 1804727.
[22] P. Shi, W. Ren, T. Zheng, Z. Ren, X. Hou, J. Peng, P. Hu, Y. Gao, Y. Zhong, P. K. Liaw, Nat. Commun. 10 (2019) 489.
[23] X. Ma, N. Li, T. Feng, L. Xiao, Mater. Res. Lett. (2025) 1–10.
[24] J. Li, X. Ma, K. Lu, Y. Wang, Y. Zhu, Acta Mater. 282 (2025) 120516.
[25] H. Mughrabi, T. Ungar, W. Kienle, M. Wilkens, Philos. Mag. A 53 (6) (1986) 793–813.
[26] F. Mompiou, D. Caillard, M. Legros, H. Mughrabi, Acta Mater. 60 (8) (2012) 3402–3414.
[27] J. Liu, C. Chen, Q. Feng, X. Fang, H. Wang, F. Liu, J. Lu, D. Raabe, Mater. Sci. Eng. A 703 (2017) 236–243.
[28] X. Ma, F. Li, J. Cao, Z. Sun, Q. Wang, J. Li, Z. Yuan, J. Alloy. Comd. 703 (2017) 298–308.
[29] C. Niu, C.R. LaRosa, J. Miao, M.J. Mills, M. Ghazisaeidi, Nat. Commun. 9 (1) (2018) 1363.
[30] J. Miao, C. Slone, T. Smith, C. Niu, H. Bei, M. Ghazisaeidi, G. Pharr, M.J. Mills, Acta Mater. 132 (2017) 35–48.
[31] M.A. Meyers, A. Mishra, D.J. Benson, Prog. Mater. Sci. 51 (4) (2006) 427–556.
[32] K. Yang, Y. Ivanisenko, A. Caron, A. Chuvilin, L. Kurmanaeva, T. Scherer, R. Z. Valiev, H.-J. Fecht, Acta Mater. 58 (3) (2010) 967–978.
[33] X. An, Z. Wang, S. Ni, M. Song, Sci. China. Mater. 63 (9) (2020) 1797–1807.
[34] S. Zhu, D. Yan, K. Gan, W. Lu, Z. Li, Scr. Mater. 191 (2021) 96–100.
[35] Z. Li, C.C. Tasan, K.G. Pradeep, D. Raabe, Acta Mater. 131 (2017) 323–335.
[36] Z. Li, K.G. Pradeep, Y. Deng, D. Raabe, C.C. Tasan, Nature 534 (7606) (2016) 227–230.
[37] D. Fahr, Metall. Trans. 2 (1971) 1883–1892.
[38] L. Fan, R. Ni, L. Ren, P. Xiao, Y. Zeng, D. Yin, H. Dieringa, Y. Huang, G. Quan, W. Feng, J. Magnes. Alloy. (2024).
[39] W. Wu, K. Gan, Q. Yang, D. Yan, Y. Zhang, Z. Li, Mater. Sci. Eng. A 900 (2024) 146511.